Charging and discharging heat transfer enhancement in a latent thermal energy storage array using petal-shaped tubes and fins

Fathi Alimi [a], Khalil Hajlaoui [b,*], Mohamed Bouzidi [c], Mansour Mohamed [c], Wahiba Yaïci [d], Nashmi H. Alrasheedi [b], Mohammad Ghalambaz [e,**], Pouyan Talebidadehsardari [f]

[a] Department of Chemistry, College of Science, University of Ha'il, P.O. Box 2440, Ha'il, 81441, Saudi Arabia
[b] College of Engineering, Imam Mohammad Ibn Saud Islamic University (IMSIU), Riyadh, Saudi Arabia
[c] Department of Physics, College of Science, University of Ha'il, P.O. Box 2440, Ha'il, Saudi Arabia
[d] CanmetENERGY Research Centre, Natural Resources Canada, 1 Haanel Drive, Ottawa, Ontario, Canada
[e] Department of Mathematical Sciences, Saveetha School of Engineering, SIMATS, Chennai, India
[f] Power Electronics, Machines and Control (PEMC) Institute, University of Nottingham, Nottingham, UK

GRAPHICAL ABSTRACT
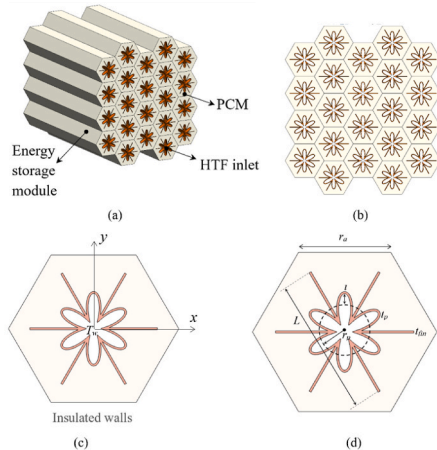
The energy storage unit and petal tube bundle. (a) a 3D view of the overall model, (b) a 2D view, (c) thermal boundary conditions, and (d) geometric dimensions.

* Corresponding author.
** Corresponding author.
    E-mail addresses: kmhajlaoui@imamu.edu.sa (K. Hajlaoui), m.ghlambaz@gmail.com (M. Ghalambaz).

ARTICLE INFO

ABSTRACT

This work presents a comprehensive numerical investigation into the enhancement of heat transfer in latent heat thermal energy storage (LHTES) arrays using petal-shaped tubes combined with copper fins. A series of 19 configurations, varying the number of petals from 3 to 6, and fin arrangements were analyzed. The results show that increasing the number of petals from 3 to 6 reduces the melting time to reach a 0.9 melting volume fraction from 102 min to 60 min and solidification time to a 0.1 melting fraction from 200 min to 100 min. The optimal configuration (6-petal tube with orizontal fins) achieved a melting fraction of 94 % after just 40 min, compared to only 91 % for the best symmetrical fin case and 57 % for the baseline circular tube, demonstrating a reduction in melting and solidification times by more than 50 %. Further, the use of petal-shaped tubes with asymmetrical horizontal fins reduced total solidification time by nearly 78 % relative to the baseline. This study provides clear design guidelines and quantitative benchmarks for optimizing LHTES units, showing that carefully engineered petal-shaped tubes and fin geometries can significantly advance thermal performance for practical applications in solar energy, waste heat recovery, and building heating systems.

Nomenclature

Symbol	Description
Latin Symbols	
A_{mush}	Mushy zone constant (Pa·s/m^2)
$A\mu$	artificial viscosity (Pa·s)
C_p	Specific heat capacity (J/kg·K)
g	gravity acceleration (m/s^2)
k	thermal conductivity (W/m.K)
L	fin length (m)
l	the petal amplitude (m)
L_{PCM}	Latent heat of fusion (J/kg)
MVF	Melting volume fraction
n	surface normal vector
N	petal number
Nm	Grid resolution factor
p	Pressure (Pa)
q	heat flux (W/m^2)
Q_{latent}	Latent heat component (J)
$Q_{sensible}$	Sensible heat component (J)
Q_{stored}	Total stored energy (J)
r_a	Hexagon length (m)
r_p	Petal base radius (m)
S	Angular coordinate for petal definition
t	*time* (s)
T_0	Initial temperature (°C)
T_f	Fusion temperature (°C)
t_{fin}	fin thickness (m)
T_{wall}	Tube wall temperature (°C)
u, v	Velocity components (m/s)
x, y	Spatial coordinates (m)
Greek Symbols	
β	Thermal expansion coefficient (1/K)
ΔT_f	Phase change temperature range (°C)
λ_{mush}	mushy parameter for denominator
μ	Dynamic viscosity (Pa·s)
ρ	Density (kg/m^3)
$\varphi(T)$	Liquid fraction as a function of temperature
Subscripts	
Fin	Copper fin
HTF	Heat Transfer Fluid
l	Liquid phase
PCM	Phase Change Material
s	Solid phase
Acronyms	
CCM	Close Contact Melting
FEM	Finite Element Method
HTF	Heat Transfer Fluid
LHTES	Latent Heat Thermal Energy Storage
PCM	Phase Change Material

1. Introduction

Latent heat thermal energy storage (LHTES) systems are becoming increasingly important as we look for better, more sustainable ways to manage energy in different industries. These systems work by using PCMs, which absorb or release heat as they change between solid and liquid states. This allows for efficient energy storage and helps keep temperatures stable. One of the main challenges with LHTES systems is the creation of "dead zones," where the PCM melts or solidifies more slowly due to uneven heat distribution. These dead zones can slow down the charging and discharging processes [1]. To tackle this problem, engineers often add metallic fins, which help distribute heat more evenly and speed up the phase change in these stubborn areas [1]. LHTES systems are especially valuable for capturing and reusing solar energy or waste heat, particularly at temperatures between 40 and 200 °C. This makes them well-suited for both home and commercial heating and cooling needs [2]. Because these systems are so versatile, they could play a big role in cutting down our reliance on limited resources like petroleum. This is especially important for countries like India, which currently has to import around 86 % of its petroleum to keep up with energy needs [2].

LHTES systems are being put to use in a wide range of areas, from solar energy and waste heat recovery to building materials, cooling technologies, textiles, and even nuclear power [3]. To get the most out of these systems, researchers are exploring different ways to boost their thermal performance. This includes improving how well heat moves through phase change materials, either by adding nanomaterials, encapsulating the PCMs, or redesigning heat transfer surfaces with things like fins or direct contact interfaces [3–5]. The design of these fins, how long they are, what angle they're set at, and what they're made of can make a huge difference in cutting down dead zones and increasing overall efficiency [1]. On top of that, advanced modeling techniques, such as temperature-based and enthalpy-based models, are helping scientists better understand how phase changes actually happen, which leads to smarter, more effective system designs [6]. All these improvements matter a lot, not just for capturing and storing solar energy, which, at the moment, taps into only about 0.023 % of the sunlight that reaches us globally, but also for reducing heat loss and making energy storage last longer. Because of this, LHTES systems are shaping up to be a key part of future sustainable energy solutions [2,4].

The shape and design of fins in LHTES systems are key to tackling the naturally low thermal conductivity of PCMs, and they have a big impact on how efficiently the materials can melt and solidify. For example, newly designed arrow-shaped longitudinal fins in horizontal shell-and-tube setups help boost both conduction and natural convection. With the right arrangement, these fins reduce the amount of unmelted PCM and enhance heat transfer by promoting stronger convective currents [7]. In another approach, using sinusoidal (wavy) fins alongside petal-shaped tubes in multi-tube LHTES units can cut melting time by up to 57 % compared to standard straight fins, clearly showing how these unique shapes can make the phase change much more efficient [8]. There are also connected Y-shaped fins modeled after natural structures like lotus leaves, which improve solidification in shell-and-tube systems and can shorten discharge times by 53.9 %, thanks to a careful optimization of the fins' positions and widths [9]. However, both corrugated/wavy and Y-shaped fins have been studied almost exclusively in single-tube or symmetric-fin layouts. These configurations accelerate melting near fin tips but leave stagnant PCM near the tube wall and between neighboring tubes, particularly during discharge when downward convection is critical. Whether asymmetric fin placement can deliberately open convective paths and reduce inter-tube shielding in a multi-tube array remains unaddressed. Sudarmozhi et al. [10] studies the melting heat transfer over a flat plate and interestingly considered the malting phenome as a part of plate boundary condition.

The geometry of the shell plays a crucial role in enhancing heat transfer in PCM-based thermal storage systems. Petal-shaped or lobed-structure enclosures increase the heat transfer surface area and promote more uniform thermal distribution compared to conventional cylindrical geometries. These features improve thermal contact between the heat transfer fluid (HTF) and PCM, accelerating melting and solidification processes. Studies have shown that using lobed tubes can reduce melting time by approximately 30.54 % compared to straight tubes, with further enhancements up to 74.26 % when combined with metal foams and nanoparticles [11]. Similarly, lobed geometries in solar thermal storage systems can shorten melting time by up to 43 %, improving the system's heat transfer rate and overall thermal performance [12]. Unlike the lobed-structure shells reported in previous studies—which reshape the outer containment and are typically applied to single-shell configurations—internal petal-shaped tubes housed within a hexagonal shell enable close-packed stacking and promote inter-tube convection pathways in multi-tube arrays. While both lobed and petal geometries increase heat transfer surface area, the petal configuration introduces high-curvature apex regions that, when paired with asymmetrical fins, can intentionally guide buoyancy-driven convection during discharge, thereby reducing stagnation pockets common in symmetric-fin designs. The ability to disrupt inter-tube thermal shielding while maintaining identical PCM volume and fin mass represents a further advantage, yet the combined influence of petal perimeter densification and fin asymmetry on array-level uniformity and discharge performance has not been reported in the literature.

The shape of the tubes used in LHTES systems plays a major role in how well these systems store and transfer heat. It affects everything from how quickly phase changes happen to how efficiently energy is stored overall. For instance, when comparing different setups like shell-and-tube, rectangular, and cylindrical units, shell-and-tube designs consistently come out on top. They offer the fastest phase change times and the best heat transfer rates, with a j/f factor that's 21.4 % higher than rectangular units and twice as high as cylindrical ones [13]. Tweaking the tube design further, such as adding different kinds of framed structures (smooth, arc-shaped, or zigzag) to vertical shell-and-tube systems, can dramatically cut down melting time by 55 % and increase thermal energy storage by 115 %. Among these, reverse arc-shaped frames are the most effective, delivering peak rates of about 34 W [14]. In systems using multi-PCM bricks, arranging rectangular inserts with different melting points improves heat exchange even more, showing that tube shape does not just impact what happens inside the system but also how it interacts with its surroundings [15]. Innovative tube designs like wavy, polygonal, and crossing patterns are taking LHTES systems to the next level by making both charging and discharging much more efficient. For example, in photovoltaic thermal systems, using wavy tubes in the collector can boost energy efficiency by up to 85 % and exergy efficiency by 14.67 %. These numbers are a significant improvement over traditional straight tubes, thanks to fine-tuning

the tubes' wavelength, amplitude, and diameter [16]. Vertical LHTES tanks that use crossing tubes set at angles up to 50° can cut melting time by 39 % and speed up solidification by 53 % compared to systems with just a single tube. This is because the angled tubes enhance natural convection and lower thermal resistance [17]. Polygonal tube systems also show impressive results, increasing heat flux by 14.53 % and power output by 21.21 % when compared to regular circular tubes. When you look at triplex-tube designs with wavy, step-like channels, the discharge process becomes 65.1 % faster, and heat recovery jumps by 147.9 %. Tweaking the shape of the waves and adjusting heat transfer fluid conditions can make these benefits even greater [18,19].

Moreover, Petal-shaped tubes are proving to be an engaging innovation in LHTES systems thanks to their strong structure and increased surface area, both of which make heat transfer much more efficient. In multi-tube LHTES setups, switching from standard circular tubes to petal-shaped ones, especially when paired with wavy fins, can speed up the melting of phase-change materials like paraffin wax RT35. For example, using tubes with nine petals cuts the charging time by 24 % compared to regular circular tubes and by as much as 57 % when compared to a basic single-tube system with straight fins [8]. This jump in performance comes from the extra surface area, which improves heat exchange, and the sturdy design, which helps the system handle thermal stress. The benefits show up in other systems, too. In shell-and-tube TES units, petal-shaped pipes increase the system's heat storage power, and the effect is even more substantial when copper nano-additives are used, boosting heat transfer by 45 % over circular tubes, mainly because the petal shape puts more of the tube in contact with the PCM [20]. With all these advantages, petal-shaped tubes are emerging as an excellent solution for tackling the usual problems of slow heat transfer in PCM-based energy storage systems. Furthermore, Petal-shaped tubes are even more impressive in LHTES units because they work so well with added enhancements like internal fins or external factors such as magnetic fields to improve heat transfer further. Simulations show that when a 4-Pl tube is fitted with internal branch fins, adjusting the fin length and narrowing the angle between fins can boost the PCM's melting performance by 18.7 %. This is mainly due to the larger surface area and better heat distribution created by the petal design [21]. The robust structure of petal-shaped tubes also makes it easy to add these features without compromising stability, while their unique shape naturally encourages both convection and conduction in the PCM. The performance gets even better when a non-uniform magnetic field is applied, with melting rates rising by another 10 %. This shows how the petal shape and external enhancements can work together for even greater results [21]. In fact, in optimized setups, the amplitude of the petal design alone can account for up to 41 % of the improvement in energy storage, much more than what nano-additives can achieve, highlighting just how critical petal-shaped tubes are for boosting the thermal performance of LHTES systems [20]. In addition, Hexagonal-shaped enclosures draw a lot of interest in thermal engineering because their unique six-sided design offers real benefits for improving heat and mass transfer, especially through natural convection. These enclosures are incredibly versatile and are used to study important heat transfer behaviours relevant to everything from industrial heat exchangers to environmental systems [22]. Studies show that the thermal performance of hexagonal cavities is heavily influenced by the Rayleigh number, which is a key factor in convection. For instance, when the Rayleigh number increases from 10^5 to 10^6, the average Nusselt number jumps by 76.16 %, indicating much stronger convective heat transfer [22].

Beyond geometric and material-based strategies, recent work has highlighted close-contact melting (CCM) as an alternative route to accelerate phase change in LHTES. Parametric studies show that CCM can contribute up to half of the overall melting rate compared to natural convection [23]. To further enhance this effect, pressure-assisted CCM has been proposed, including magnetically regulated designs that reduce interfacial resistance and improve thermal charging under high heat fluxes [24]. Similarly, pressure-driven CCM buffers have demonstrated faster melting and improved temperature uniformity, making them promising for high-power electronic cooling [25]. More dynamic approaches—such as weighted "hourglass" systems—extend CCM principles by continuously forcing solid PCM against the heat source, achieving robust and cyclic operation [26]. Recent modeling also clarifies how thin-layer convection modifies CCM behavior under varying external forces and heat flux conditions [27].

Petal-shaped tubes introduce high-curvature apex regions that, when paired with asymmetrical fins, can deliberately guide buoyancy-driven convection during discharge—reducing stagnation pockets common in symmetric-fin designs. Moreover, placing these tubes within a hexagonal shell enables close-packed multi-tube arrays, where fin asymmetry can disrupt inter-tube thermal shielding and improve array-level uniformity under identical PCM volume and fin mass constraints.

This study addresses these gaps by conducting the first constant-mass, constant-PCM-volume parametric investigation of petal-shaped tubes with both symmetric and asymmetric horizontal copper fins in a hex-packed multi-tube LHTES array. The study examines how petal number and fin arrangement influence melting/solidification rates, convection pathways, and array-level uniformity under identical material budgets, directly targeting the unresolved issues of low heat transfer rates, non-uniform melting, and unquantified petal–fin interaction effects in prior designs.

2. Physical model

2.1. Model description

Solar energy can be transformed into heat and stored in LHTES units, which are space-efficient, economical, and environmentally sustainable. These systems offer long service life, minimize the reliance on costly chemical batteries, and facilitate the use of renewable energy in building applications. Consider a solar thermal system designed to supply hot water by incorporating an LHTES unit. The selected PCM melting temperature range of 49 °C–54 °C aligns with typical operating temperatures of domestic solar hot-water systems, where outlet water is commonly maintained between 50 °C and 60 °C for hygienic and comfort purposes. This range ensures effective charging from solar collectors under moderate solar flux conditions and efficient discharging to meet hot water demand without auxiliary reheating.

A solar collector captures sunlight to heat water, which is circulated through a storage tank by a pump, raising the tank's water

temperature. A secondary pump transfers water between the LHTES unit and the tank, thereby charging the thermal storage. The tank then delivers hot water to the building. When hot water demand rises or solar energy is unavailable, the water temperature in the tank may fall below the LHTES phase change temperature. Under these conditions, water circulates between the tank and the LHTES unit, releasing the stored energy and maintaining a steady water temperature to ensure a consistent hot water supply. Based on the described cycle, during the discharging phase, the LHTES releases heat to the circulating water, while in the charging phase, it absorbs heat from the circulating water. In this study, the solid PCM is assumed to remain stationary during melting and solidification. Sedimentation or settling of the solid phase is not considered, consistent with the constrained melting assumption used in many numerical studies. It is acknowledged that in practice such effects can significantly impact heat transfer, and should be addressed in future work for more realistic system predictions.

Although LHTES units can store a large amount of thermal energy, their relatively low thermal performance can limit how well they work in energy systems. That's why finding ways to improve heat transfer is important to make them more efficient. Petal-shaped tubes help by providing more surface area, which makes it easier for heat to move through the PCM. Attached fins further enhance this effect by providing additional surface area. Since phase change is influenced by natural convection, fins can either promote or hinder this process depending on their placement. As a result, the interaction between natural convection and the extended surfaces introduced by fins and petal-shaped tubes creates complex heat transfer behavior. These coupled effects can be effectively analyzed using computational fluid dynamics simulations. It is important to highlight that certain variants of semi-circular petal-shaped tubes have already been fabricated and are commercially accessible [28].

This study explores how using petal-shaped tubes can improve the thermal performance of LHTES units. A set of petal-shaped tubes arranged within shell-type LHTES units is used for thermal energy storage, in the present study. To further improve heat transfer during the melting and solidification phases, fins are attached to support the petal-shaped tubes. Inside these tubes, a HTF circulates, exchanging heat with the phase change material in the storage area. Fig. 1(a) provides a schematic illustration of this configuration. The space between the tubes is filled with PCM and fins. During the charging phase, the hot HTF flows through the petal-shaped tubes and transfers heat to the adjacent PCM primarily through conduction, causing the PCM to melt. As the PCM transitions to a liquid state, natural convection within the PCM region becomes more significant, triggering convective flow.

During the energy release process, the cold fluid passes through the petal-shaped tubes, causing the molten PCM surrounding them to start solidification. Since some hot liquid PCM remains, natural convection effects are expected, with downward convection currents
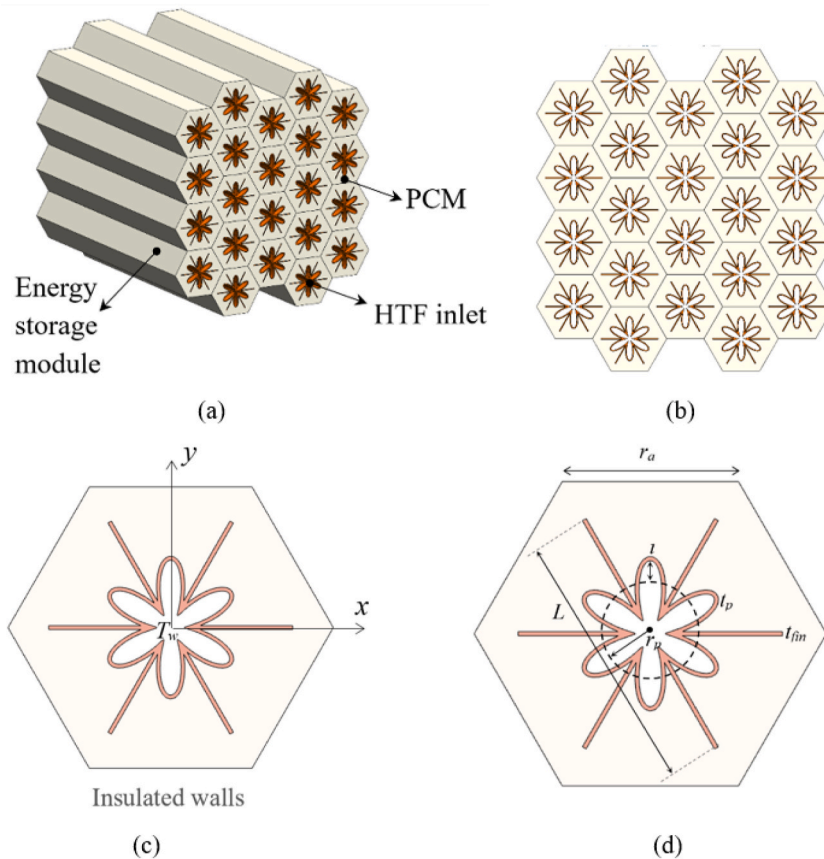

Fig. 1. The energy storage unit and petal tube bundle. (a) a 3D view of the overall model, (b) a 2D view, (c) thermal boundary conditions, and (d) geometric dimensions.

forming in the molten region. Fig. 1(a) presents a 3D view of the overall model, where boundary effects are neglected under the assumption of long tubes. At high HTF flow rates, the inner tube walls can be assumed to maintain a constant temperature. This isothermal wall assumption is commonly used in numerical LHTES studies to isolate PCM-side heat transfer mechanisms. In practice, achieving such uniform tube-wall temperatures would require sufficiently high HTF flow rates, which may incur additional pumping power and may not always be optimal for overall system efficiency. Therefore, the present results should be interpreted as an upper bound for thermal performance, with future work recommended to include conjugate HTF–PCM heat transfer and pumping power analysis for more comprehensive assessment under realistic operating conditions.

Based on these assumptions, the thermal energy storage within the tube bundle is modeled as illustrated in Fig. 1(b). Moreover, the thermal conditions along with the geometric dimensions are shown in Fig. 1(c) and (d). As shown in Fig. 1(b), the hexagonal structure is well-suited for stacking energy storage modules, as they fit seamlessly next to one another without wasted space. Beyond this practical packing advantage, the hexagonal shell geometry can also influence PCM thermal behavior. Compared to a circular shell, the flat walls of a hexagon shorten the average conduction path from the tube bundle to the shell boundary and can promote more uniform heat distribution within the PCM. The corners may create localized regions of reduced natural convection, but in the present multi-module arrangement these effects are mitigated by inter-tube flow circulation and stacking effects.

The petal is reinforced with copper fins placed at various lengths and locations. In every scenario, the total mass of the fins remains constant. The petal's shape is defined by a polygon, specified using the given x and y coordinates as follows:

$$\begin{cases} x = (r_p + l\, sin(S.N))cos(S) \\ y = (r_p + l\, sin(S.N))sin(S) \end{cases} \tag{1}$$

where $S = [0.0, 0.03, 0.06, \ldots, 2\pi]$. The area of petal and mass of fins remains fixed in all cases. Thus, the amount of PCM in all cases is the same. The fin thickness and length are t_{fin} and L, respectively. The characteristics length was considered as the hexagon length ($r_a = 7/4$ inch). The petal base circular radius is considered fixed as $r_p = r_a/4$, petal amplitude is l, and the petal number is N. The inner petal area is computed as 4.74E-4 m^2, and the hexagon area is 5.13E-3 m^2 which gives a petal area to hexagon area as 0.0924. Petal tube thickness is 1 mm, and the fin length $L = 3r_a/2$. The default fin thickness is considered as $t_{fin} = 1.07$ mm which gives a fin area of 1.725E-4 m^2. As the number of fins changes, the fin thickness can be changed to keep the amount of fin mass fixed.

2.2. Governing equations and mathematical formulation

In this section, the governing equations of the Phase change material zone are presented. There is conduction heat transfer in solid fins and petal wall while, natural convection is assumed to occur within the molten PCM. The natural convection flow in liquid PCM is laminar and incompressible. It is assumed the flow velocity and convective heat transfer inside the tube is high and the tube temperature is considered at a fixed isothermal temperature T_{wall}. Therefore, the continuity and momentum equations are used for the PCM zone. Furthermore, the modeling of the phase change is carried out via the enthalpy-porosity approach. additional source terms are used to the momentum equations for ensuring zero velocity in the solid PCM as a function of liquid fraction (φ). Due to the small changes in the temperature field in this research, the properties of material are as a function of temperature only for PCM. The changes in the thermophysical properties are due to the phase change. Moreover, the Boussinesq approximation is applied to consider the density change in the liquid PCM.

The governing equations including the continuity, momentum, and energy equations are expressed in the differential form as follows [29–31]:

$$\left(\frac{\partial u}{\partial x} + \frac{\partial v}{\partial y}\right) = 0 \tag{2}$$

$$\rho_{PCM}\frac{\partial u}{\partial t} + \rho_{PCM}\left(u\frac{\partial u}{\partial x} + v\frac{\partial u}{\partial y}\right) = -\left(\frac{\partial p}{\partial x}\right) + \left[\frac{\partial}{\partial x}\left(\mu_{PCM}\frac{\partial u}{\partial x}\right) + \frac{\partial}{\partial y}\left(\mu_{PCM}\frac{\partial u}{\partial y}\right)\right] - A_{mush}\frac{(1 - \varphi(T))^2}{\lambda_{mush} + \varphi^3(T)}u \tag{3a}$$

$$\rho_{PCM}\frac{\partial v}{\partial t} + \rho_{PCM}\left(u\frac{\partial v}{\partial x} + v\frac{\partial v}{\partial y}\right) = -\left(\frac{\partial p}{\partial y}\right) + \left[\frac{\partial}{\partial x}\left(\mu_{PCM}\frac{\partial v}{\partial x}\right) + \frac{\partial}{\partial y}\left(\mu_{PCM}\frac{\partial v}{\partial y}\right)\right] + g\rho_{PCM}\beta_{PCM}(T - T_0) - A_{mush}\frac{(1 - \varphi(T))^2}{\lambda_{mush} + \varphi^3(T)}u \tag{3b}$$

$$(\rho C_p)_{PCM}\frac{\partial T_{PCM}}{\partial t} + (\rho C_p)_{PCM}\left(u\frac{\partial T_{PCM}}{\partial x} + v\frac{\partial T_{PCM}}{\partial y}\right) = \frac{\partial}{\partial x}\left(k_{PCM}\frac{\partial T_{PCM}}{\partial x}\right) + \frac{\partial}{\partial y}\left(k_{PCM}\frac{\partial T_{PCM}}{\partial y}\right) - \rho_{PCM}L_{PCM}\frac{\partial \varphi(T)}{\partial t} \tag{4}$$

where L_{PCM} is the enthalpy of fusion, β denotes the coefficient of heat volume expansion, and g is the gravity. The melting process in this study is classified as constrained melting, where the solid PCM remains stationary and cannot shift or settle to the bottom of the container. The phase change occurs in place, with the solid structure retained throughout the melting process [32].

In order for the solid phase to follow the zero-velocity law, a term is added to the momentum equations including two factors of $A_{mush} = 10^6$ Pa s/m^2 and $\lambda_{mush} = 10^{-3}$ were selected directly from well-established literature [33–35]. The possible values of A_{mush} was studied by Karami and Kamkari [34] and Arena et al. [35]. During a melting process, as A_{mush} reduces, the melting interface slightly shifts toward the solid region [34,35]. A considerably large magnitude of A_{mush} ensures that the flow solution is primarily influenced by the solid zones. Furthermore, λ_{mush} is assigned a small value to avoid zero division. The PCM's viscosity is stated as $\mu = A\mu(1-\varphi) + \mu_{PCM,l}\,\varphi$ where φ denotes the liquid volume fraction and $A\mu$ is a coefficient with large amount (10^4 Pa s). Additionally, the

temperature-dependent liquid volume fraction is expressed as follows [36]:

$$\varphi(T) = \begin{cases} 0 \ T < -\dfrac{1}{2}\Delta T_f + T_f \text{(Solid)} \\ \dfrac{1}{2} + \dfrac{(T - T_f)}{\Delta T_f} - \dfrac{1}{2}\Delta T_f + T_f \leq T \leq \dfrac{1}{2}\Delta T_f + T_f \text{(Mixture)} \\ 1 \ T > \dfrac{1}{2}\Delta T_f + T_f \text{(Liquid)} \end{cases} \tag{5}$$

where ΔT_f is the solid and liquid temperature difference ($\Delta T_f = 54°C - 49°C$). The thermophysical properties of the PCM are calculated using a linear interpolation as follows:

$$f(\rho C_p)_{\text{PCM}} = (1 - \varphi)(\rho C_p)_l + \varphi(\rho C_p)_s \tag{6a}$$

$$\rho_{\text{PCM}} = (1 - \varphi)\rho_l + \varphi\rho_s \tag{6b}$$

The subscript s denotes the solid phase while, l represents the liquid phase of PCM. The values of density, thermal conductivity, and specific heat capacity are presented in Table 1 for the paraffin as PCM, and copper as tube material. The energy conservation in the fin and petal tube wall is explained by:

$$(\rho C_p)_{Fin}\frac{\partial T_{Fin}}{\partial t} = k_{\text{Fin}}\left(\frac{\partial}{\partial x}\left(\frac{\partial T_{Fin}}{\partial x}\right) + \frac{\partial}{\partial y}\left(\frac{\partial T_{Fin}}{\partial y}\right)\right) \tag{7}$$

where the subscript Fin indicate the fins and petal tube.

The phase change material has a melting temperature range of 49 °C–54 °C and a latent heat of 1.76×10^5 J/kg, as reported in Ref. [37]. Its dynamic viscosity and thermal expansion coefficient, valued at 3.6×10^{-3} kg/m·s and 9.0×10^{-4} (1/K), respectively, were also obtained from Refs. [37–39]. The fusion temperature is taken as T_f=(49 °C + 54 °C)/2 = 51.5 °C.

2.3. Boundary and initial conditions

The tube wall is maintained at a high temperature of $T_{wall} = T_f + 15$ °C. All other walls are insulated, preventing any heat flow (–n·q = 0). No-slip boundary conditions are applied to every wall surface. The heat flux and temperature continuity were applied at the solid-PCM interfaces. The initial temperature of the system is set to $T_0 = T_f - 15$ °C, and a reference point with zero relative pressure is established at the lower left corner of the container.

2.4. Desired parameters

The quantity of melted PCM is represented by the melting volume fraction, which is calculated as follows:

$$MVF = \frac{\oint_V \varphi dV}{\oint_V dV} \tag{8a}$$

where dV denotes the volume element of shell domain.

The total stored thermal is the combined sum of sensible and latent heat, calculated as follows:

$$Q_{sensible} = \left[\oint_{V_{\text{PCM}}}\left(\int_{T_0}^{T_{PCM}}(\rho C_P)_{\text{PCM}}dT\right)dV\right] + (\rho C_P)_{\text{Fin}}\oint_{V_{\text{Fin}}}(T_{\text{Fin}} - T_0)dV \tag{8b}$$

$$Q_{latent} = \oint_V \rho_{\text{PCM}}\varphi L_{\text{PCM}}dV \tag{8c}$$

Therefore:

$$Q_{stored} = Q_{sensible} + Q_{latent} \tag{8d}$$

Table 1
Thermophysical Properties of PCM and tube materials.

Materials	ρ (kg/m³)	k (W/m.K)	C_p (J/kg.K)
Paraffin (solid/liquid) [37–39]	916/790	0.21/0.12	2700/2900
Copper [40]	8900	380	386

3. Numerical procedure and its verifications

This section presents an overview of the numerical approach employed, examines the impact of mesh refinement, and outlines the procedures used to assess the model's reliability.

3.1. Finite element procedure

The fundamental equations, together with their initial and boundary conditions are solved using the finite element method (FEM). This computational approach is chosen for its effectiveness in handling the complex source and sink terms associated with the melting and solidification processes [41,42]. The momentum and energy equations are discretized into second-order forms. Utilizing Gauss quadrature at the element level yields a set of algebraic residual equations. These residuals are solved iteratively using a coupled Newton-Raphson method [43,44], stabilized by a damping factor of 0.9 to promote smoother convergence. Because the calculations are extensive, we incorporated the PARDISO parallel scheme, which takes advantage of multicore processors to speed computations up [45,46]. We also carefully manage the simulation timesteps using backward differential formula (BDF) to automatically update the timestep, and making sure the difference between updates stays below a relative error of 0.0001 [5,33,47,48]. An absolute scaled error of 10^{-6} was applied to monitor the convergence. To keep solutions, stable numerically, we use a backward difference method.

The simulation is set to stop once the phase transition is almost complete. For melting cases, the calculation ends when the MVF exceeds or reaches 0.99. For solidification problems, the simulation concludes when the MVF drops below 0.01. Fig. 2 shows an overview of the entire computational process.

3.2. Grid independence study

A grid independence study is carried out for the Case 16. The melting and solidification process is investigated for several grid sizes. An unstructured grid is used for the domain discretization. The grid size is controlled via a grid resolution factor called *Nm*. This
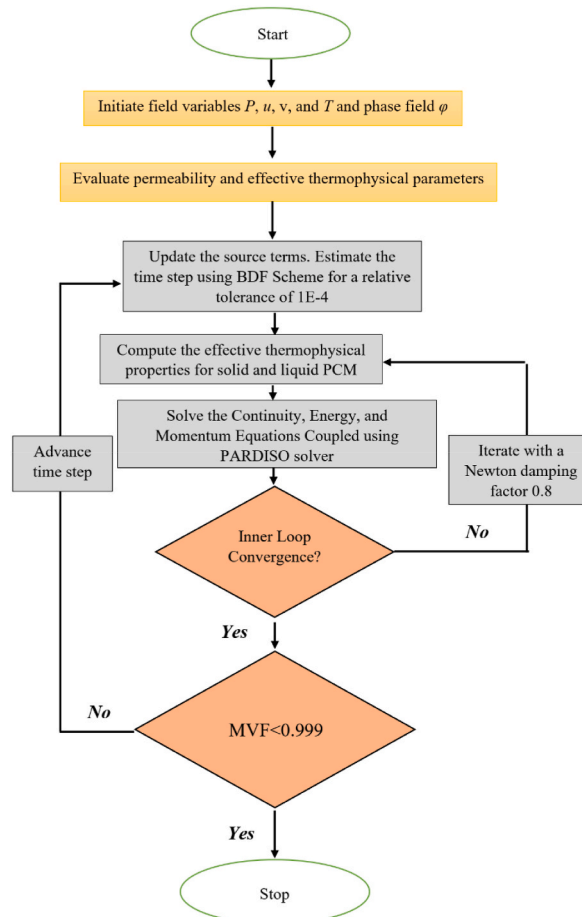

Fig. 2. Flowchart of the numerical method used for simulating phase change in LHTES.

quantity directly affects the grid density, which in turn impacts both the simulation's accuracy and computational time. Table 2 summarizes the grid characteristics corresponding to various *Nm* values, detailing the number of edge elements, triangles, and total elements for each grid configuration. A non-uniform triangular grid is employed. Also, the grid elements are linked across the periodic boundaries to make sure that matching structures on opposite edges are aligned properly, which helps improve both accuracy and the stability of the solver.

Fig. 3 depicts the MVF in melting and solidification states for various grid sizes. The results across different grid sizes are found to be very consistent with each other. As the grid becomes finer, the outcomes gradually converge, showing that increasing the resolution further only leads to slight gains in accuracy. In fact, the curves for grid sizes of *Nm* = 4, 5, and higher are close together, indicating that refining the grid beyond this point does not offer much-added value. Taking both accuracy and computation time into account, a grid size of *Nm* = 5 is chosen for the simulations. The error percentage is computed by reference to *Nm* = 6 as % Error = 100 × (MVF-MVF$_{@Nm = 6}$)/MVF$_{@Nm = 6}$, and the results are listed in Table 2. As seen, case Nm = 5 has only 0.5 % error compared to reference case of *Nm* = 6. Thus, the results at *Nm* = 5 are almost indistinguishable from those with finer grids, it is concluded that this resolution provided the best performance without unnecessary computational cost.

Fig. 4 shows the grid selected for the simulation, using a resolution parameter of *Nm* = 5, at several key areas, including the petal tips, edges, and domain boundaries. As can be seen, the grid is finer near the petal edges, which helps to accurately capture their complex shapes. This added detail is important for representing the petal geometry faithfully in the simulation. In addition to the refinement around the petals, a fairly fine mesh was also applied along the edges and throughout the interior of the domain. This is especially important because the phase change occurs and moves through this internal region. A higher grid resolution allows the simulation to track the details of the phase transition more precisely. Overall, the grid setup helps strike the right balance between capturing important physical details and maintaining computational efficiency.

3.3. Validation study

To validate the numerical model, the simulated temperature histories were compared against experimental data obtained from the test apparatus described in Ref. [49]. Specifically, temperature readings from thermocouples T3, T12, T21, and T30 were selected for comparison due to their representative positions within the PCM. These thermocouples capture the transient thermal behavior of lauric acid under the influence of different boundary conditions and inclination angles. The experimental setup ensured high accuracy through the use of T-type thermocouples with fine wire diameters, and the well-insulated Plexiglass enclosure minimized external thermal disturbances. In all validation cases, the enclosure was initially filled with solid lauric acid at 25 °C, and the experiments were conducted under controlled ambient conditions. The numerical model was evaluated under the same thermal boundary conditions as those imposed in the experiments, including constant wall temperatures of 70 °C. Results are plotted in Fig. 5 and show that the computed temperature profiles closely matched the experimental data throughout the melting process. The observed agreement demonstrates that the model accurately captures both heat transfer and phase change phenomena within the PCM, supporting its reliability for further parametric studies. Kamkari and Groulx [50] melting of lauric acid PCM in a fin assisted enclosure of size 5 cm × 12 cm. The PCM was supper cooled using water at 25 °C. Then melting process was carried out using 60 °C water. During melting, photographs were taken every 5 min by removing the front insulation of the enclosure. Fig. 6 depicts a comparison of melting interface for the simulations of the present study and the experiments of [50]. The region adjacent to the right wall and the fins, where hot water circulates, melts rapidly. Additionally, the upper part of the enclosure exhibits faster melting due to natural convection effects. Overall, the experimental observations and numerical simulations demonstrate good agreement, confirming the accuracy of the model in capturing the melting behavior.

4. Results and discussions

Table 3 presents a comparative analysis of 19 different LHTES unit configurations, evaluating their melting and solidification performance based on the time required to reach specific MVF. The performance metric is the time taken to reach MVF = 0.9 for melting and MVF = 0.1 for solidification, with lower times indicating better thermal response. The number of petals (*N*) ranges from 3 to 6, and both symmetrical and asymmetrical fin arrangements are considered. Notably, cases C8 to C14 incorporate asymmetrical fins, while the rest use symmetrical configurations.

As an LHTES system charges, the MVF rises from 0 (fully solid) to 1.0 (fully liquid). The process of melting slows considerably as it nears completion, making it impractical to reach an MVF of 1.0. For this reason, an MVF of 0.9 is a standard benchmark for evaluating charging performance. Conversely, during discharging, the MVF decreases from 1.0 to 0. A value of 0.1, which signifies 90 %

Table 2
Grid characteristics corresponding to various *Nm* values.

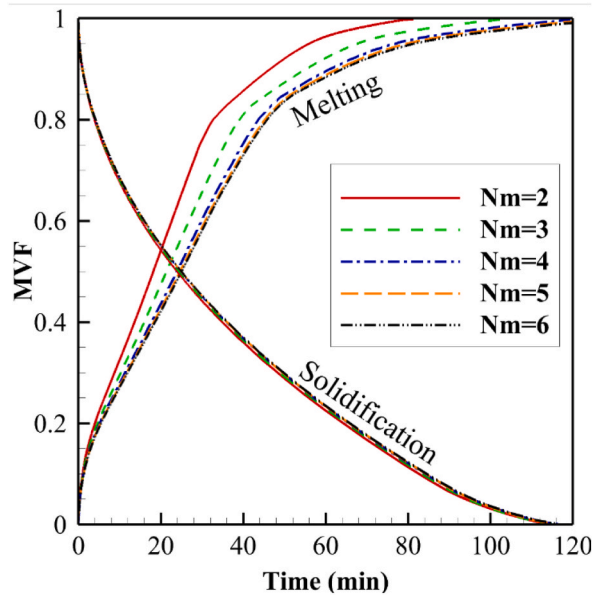| Nm	PCM	Solid Wall	Total (Entire geometry)	MVF during melting at 60 min	% Error
2	17253	7451	24704	0.964	9.0
3	26224	9210	35434	0.922	4.3
4	35875	10620	46495	0.895	1.2
5	**46776**	**11753**	**58529**	**0.888**	0.5
6	58898	13139	72037	0.884	0.0

Fig. 3. Variation of MVF in melting and solidification states with respect to time for several *Nm* factors.
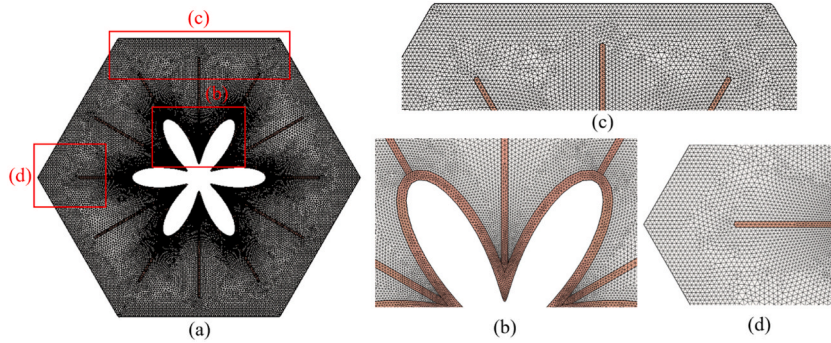

Fig. 4. Different views of selected computational grid. (a) full domain, (b) petal zone, (c) and (d) around fins.

solidification, is the typical practical reference for judging discharging behavior. These two thresholds—0.9 for melting and 0.1 for solidification—are commonly used in research to evaluate the performance of LHTES systems [51,52].

The C19 case with a circular inner tube and the same hexagonal shell is used as a baseline to evaluate these effects quantitatively. Melting performance varies significantly across the cases. The baseline case, C19, exhibited the longest melting time at 22,682 s. In contrast, C11, C15, and C16 showed the fastest melting, requiring just 2136 s, 2240 s, and 2223 s respectively—representing an approximate 90 % reduction in melting time compared to C19. Among the symmetrical configurations, an increase in petal number from 3 to 6 (from C1 to C4) resulted in a melting time reduction of about 40 %, from 6187 s to 3703 s. Asymmetrical configurations with optimized fin arrangements, particularly C11, outperformed many symmetrical designs.

Solidification time followed a similar trend, with the worst performance again seen in C19 (27900 s). C11, C15, and C16 emerged as top performers here as well, achieving solidification in 2690 s, 2848 s, and 2833 s respectively. These times reflect a dramatic improvement—over 90 % reduction—compared to the baseline. A clear correlation was observed between increasing petal count and improved solidification performance in symmetrical cases, where the time dropped from 11993 s in C1 ($N = 3$) to 5814 s in C4 ($N = 6$). Asymmetrical fin configurations also contributed to efficiency gains, particularly in finely tuned arrangements like C13 and C14.

It can be seen that both geometrical optimization and fin configuration significantly affect the thermal performance of LHTES units. Higher petal numbers, reduced fin thickness, and especially the use of asymmetrical fins in specific arrangements (such as in C11) can greatly enhance melting and solidification rates. Cases like C11, C15, and C16 achieved more than 85–90 % improvement over the baseline, highlighting the potential for substantial efficiency gains in thermal energy storage design. These findings underscore the importance of configuration-specific customization to maximize heat transfer effectiveness.

Fig. 7 shows the temporal variations of the melting volume fraction for four configurations (C1 to C4), each with a different number of petals, where the number of fins equals the number of petals. The time required to reach a MVF of 0.9 for cases C1 to C4 is 102, 89,
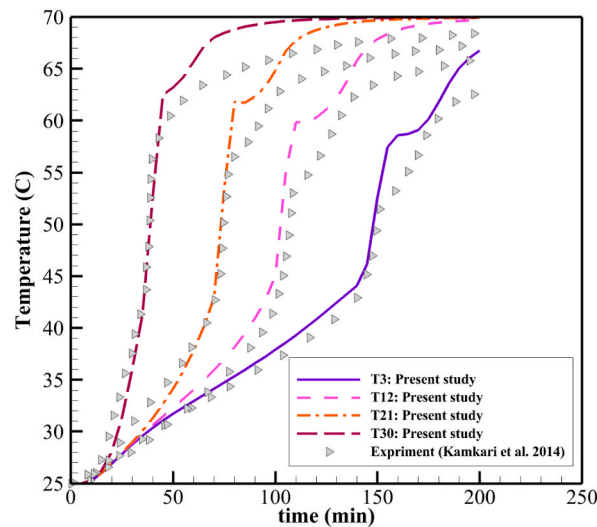
Fig. 5. Comparison between the measured temperatures from Ref. [49] and the computed temperature profiles obtained in the present study.

72, and 60 min, respectively. This indicates a progressive decrease of approximately 41 % in melting time from C1 to C4 as the number of petals increases from 3 to 6. For example, C4 melts 12 min faster than C3 (a 16.7 % improvement) and 42 min faster than C1 (41.2 % faster melting). This performance enhancement is attributed to the increased heat transfer surface area provided by additional petals and fins.

In the solidification process, the time to reach an MVF of 0.1 for C1 to C4 is 200, 147, 108, and 100 min, respectively. Similar to the melting behavior, there is a 50 % reduction in solidification time from C1 to C4. C4 solidifies 47 min faster than C2 (32 % improvement) and a substantial 100 min faster than C1 (exactly 50 % faster). These improvements clearly demonstrate that increasing the number of petals significantly enhances both charging (melting) and discharging (solidification) performance due to more efficient heat conduction pathways.

Moreover, the results confirm that the solidification process takes longer than the melting process in all cases. For instance, in C1, solidification takes 96 % longer than melting (200 vs. 102 min), while in C4, it takes about 66.7 % longer (100 vs. 60 min). This trend highlights the inherently slower heat removal rate during solidification, which is a common challenge in PCMs.

Fig. 8 supports these observations by presenting MVF contours and liquid PCM streamlines at 40 min. It is evident that the C4 case has a significantly larger melted volume than the others, consistent with its faster melting rate. Additionally, the fins not only improve thermal conduction but also influence the fluid flow patterns. Due to their role as obstacles, they create a positive pressure gradient in the flow, resulting in vortex-shaped streamlines. These vortex structures enhance heat transfer by continuously transporting hotter liquid PCM away from the heated surfaces and bringing cooler PCM toward them, increasing the effective thermal conductivity of the melt zone. However, if the vortices remain confined and fail to connect with the bulk liquid, they may cause localized recirculation without significantly expanding the melted region, thereby limiting their contribution to overall melting efficiency. This interaction between geometry and flow enhances convective mixing, further improving the thermal response of the storage unit.

The solidification process is consistently slower than the melting process due to fundamental differences in heat transfer mechanisms. During melting, a liquid PCM layer quickly forms around the heat transfer surfaces—such as the tube and fins. As this molten layer thickens, natural convection currents develop within the liquid PCM, significantly enhancing heat transfer and accelerating the melting process. In contrast, during solidification, a solid PCM layer forms first around the tube and fins and remains in place, acting as a thermal resistance barrier that impedes further heat transfer to the remaining liquid PCM. Heat transfer through this solid layer occurs primarily by conduction, which is significantly less efficient than the convective heat transfer observed during melting.

While limited natural convection may still occur in the remaining liquid PCM regions, the temperature gradient between the solid-liquid interface and the liquid domain is typically small. As a result, convection plays a minor role, and the overall heat transfer remains dominated by conduction through the solid layer. This restricted heat flow leads to a slower release of latent heat and, consequently, a slower solidification process. Therefore, the inherent difference in heat transfer modes—convection-enhanced melting versus conduction-dominated solidification—explains why solidification consistently lags behind melting in terms of thermal response.

The next study compares the melting and solidification performance of PCM in the case C4 (previously analyzed) with three symmetrical cases C5 to C7, as shown in Fig. 9. All of these cases have 6 petals, however have different petal angles and fin arrangements. The difference between the C4 and C5 cases is that the C5 case is rotated 30° relative to the C4, and the same applies to the C6 and C7. In the melting process, there is no significant difference between the results; however, the C5 case seems to be achieved a better result. In the solidification process, the difference between the curves is greater and C5 configuration still performs better. Furthermore, Fig. 10 compares the melting fraction of case C4 with three asymmetric cases C8 to C10. In the melting process, up to MVF = 0.9, the results of C4 are similar to C10, and after that, the C10 case shows a relatively better performance. However, in the
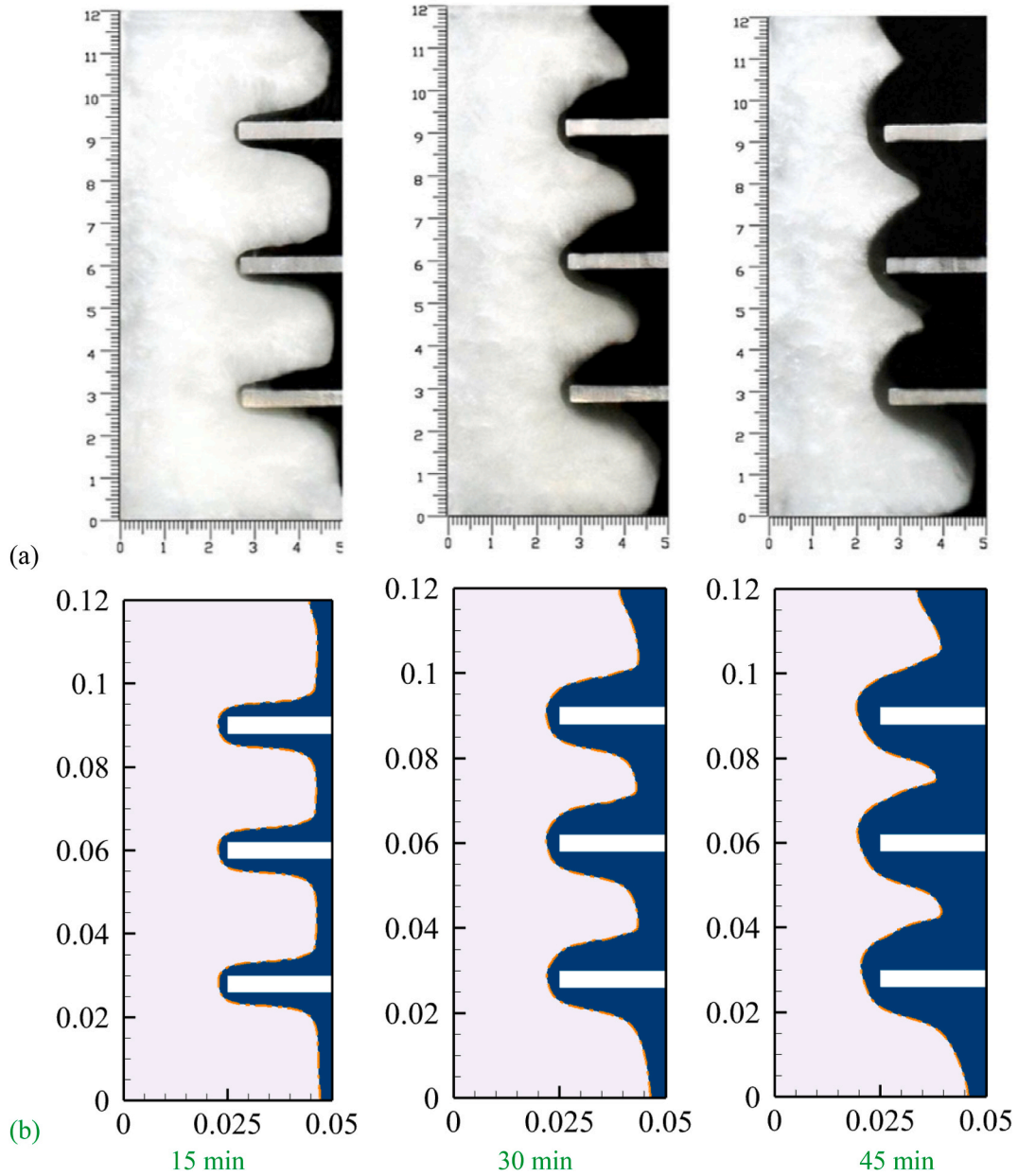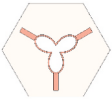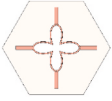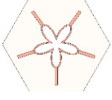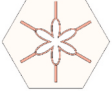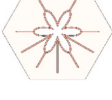
Fig. 6. Evolution of the solid–liquid interface at three selected time intervals: (a) experimental observations by Kamkari and Groulx [50] for a finned enclosure and (b) the simulations of the present study.

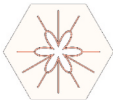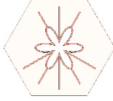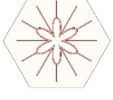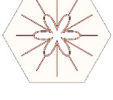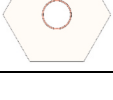solidification state, the C4 has a better result.

During the melting process, the liquid PCM surrounding the petal tube and fins is heated and rises due to natural convection. This upward flow enhances heat transfer in the upper region of the enclosure. However, at the bottom, heat transfer is relatively weak, relying primarily on conduction and cooler liquid PCM returning from the top. To address this limitation, placing asymmetric fins at the bottom can significantly improve heat transfer in that region, thereby enhancing the overall melting performance. In asymmetric configurations, the intentional disruption of flow symmetry encourages convection cells to penetrate into low-flow regions, particularly at the enclosure bottom. This breaks the vertical stratification of temperature, reduces thermal dead zones, and improves the utilization of the entire PCM volume during both melting and early solidification. The bottom-placed asymmetric fins not only increase the heat transfer surface area but also help trap localized natural convection currents, promoting additional melting at the lower part of the enclosure. Their extended length effectively channels heat deeper into the PCM, accelerating the melting process in zones that would otherwise remain colder for longer periods. During solidification, asymmetric fins also demonstrate good performance, particularly during the initial and middle stages. Their increased surface area provides more contact for the formation of solid PCM,

Table 3

Geometrical properties and melting and solidification times for each case study.

Case	t_{fin} (mm)	N	Arrangement	Melting time (s) for MVF = 0.9	Solidification time (s) for MVF = 0.1	Image
C1	4.18	3	1	6187	11993	
C2	3.13	4	1	5255	8655	
C3	2.49	5	1	4406	6586	
C4	2.08	6	1	3703	5814	
C5	2.08	6	2	3676	4844	
C6	1.12	6	1	3720	5068	
C7	1.12	6	2	3883	5927	
C8	1.63	6	1	4219	9148	
C9	1.34	6	2	3946	6301	
C10	1.2	6	1	3630	6291	
C11	1.08	6	2	2136	2690	
C12	1.29	6	2	3533	6335	

Table 3 (*continued*)

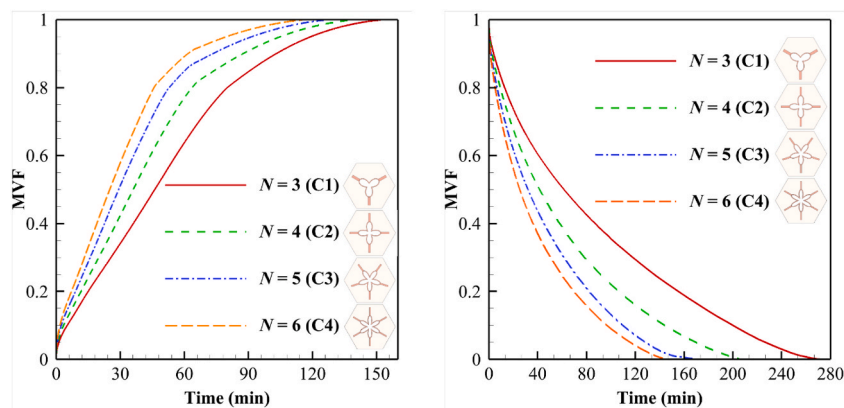| Case	t_{fin} (mm)	N	Arrangement	Melting time (s) for MVF = 0.9	Solidification time (s) for MVF = 0.1	Image
C13	0.93	6	2	2520	3707	
C14	1.1	6	2	3521	6082	
C15	0.72	6	1	2240	2848	
C16	0.72	6	1	2223	2833	
C17	–	6	2	12814	16254	
C18	–	6	1	13529	16302	
C19	–	–	–	22682	27900	

Fig. 7. Temporal variation of melting volume fraction for C1 to C4, (left) melting process, (right) solidification process.

facilitating faster heat extraction. This leads to a more efficient solidification process in the early phases when liquid PCM still surrounds much of the structure.

However, in the final stages of solidification, the benefits of asymmetric fin placement diminish. As thick solid layers build up around the tube and fins, the uneven fin distribution introduces greater thermal resistance—especially toward the upper regions of the enclosure. This results in thermal "dead zones", where heat extraction is inefficient, ultimately prolonging the total solidification time.

Next, the C4 is compared with C11 to C14 cases as shown in Fig. 11. These cases have an asymmetrical fin configuration. They differ from the cases in Fig. 10 in that they have a larger number of fins. As can be seen, the C11 achieves higher thermal efficiency than other cases and reaches a melting fraction of 0.9 in less time. This is also true for the solidification process. The configuration of the C13 case
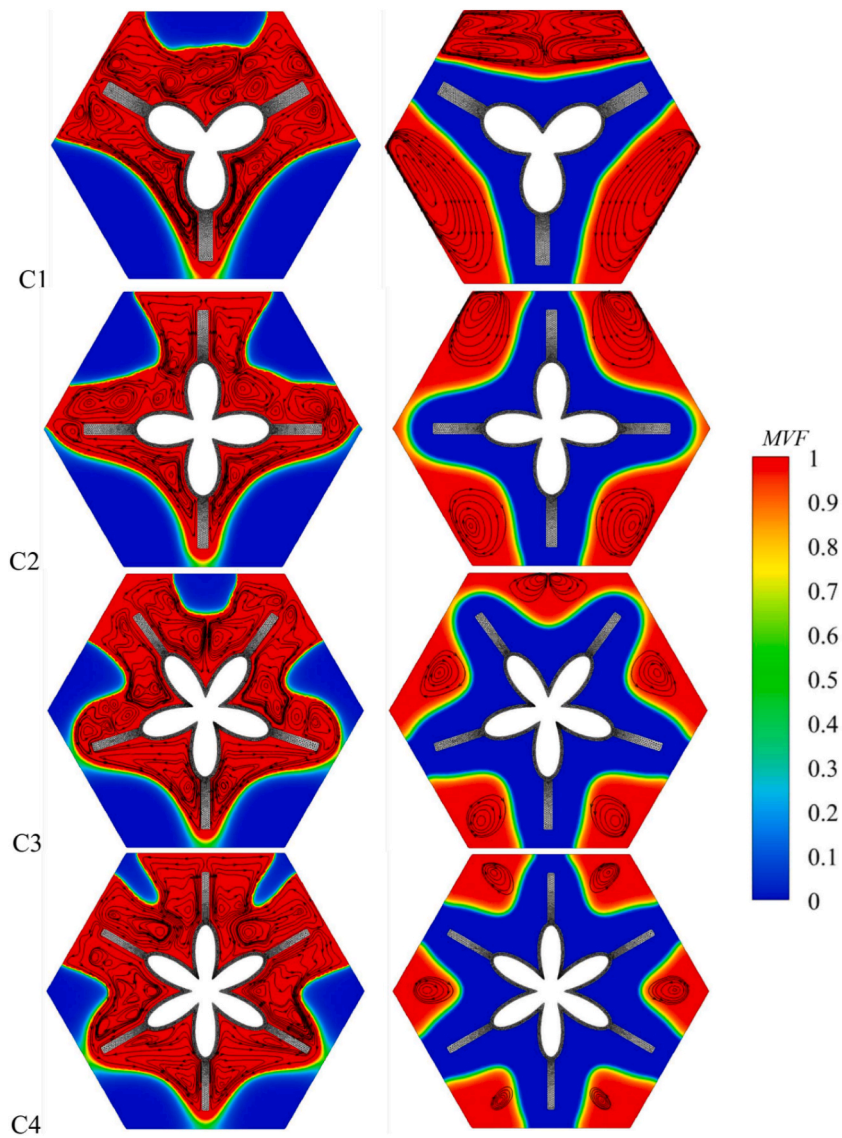
Fig. 8. Contours of MVF along with the liquid PCM streamlines at $t = 40$ min for C1 to C4, (Left) melting process, (Right) solidification process.
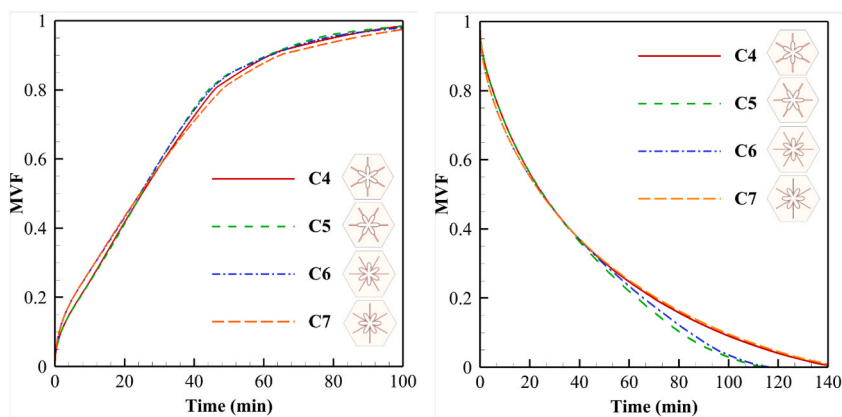

Fig. 9. Temporal variation of melting volume fraction for C4 to C7, (left) melting process, (right) solidification process.
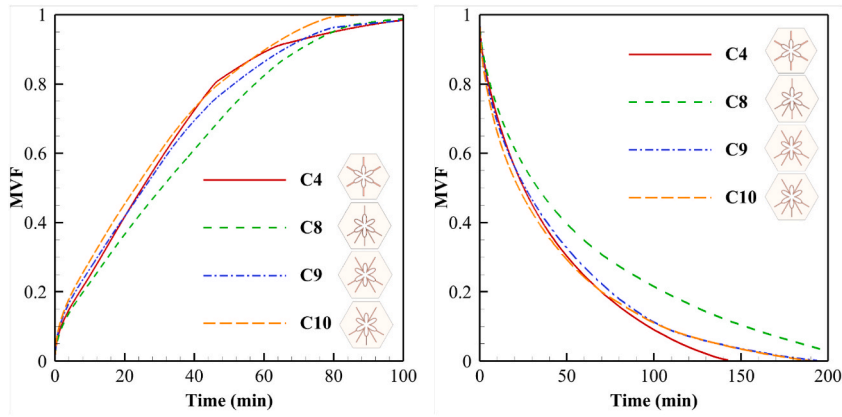
Fig. 10. Temporal variation of melting volume fraction for C4, C8, C9, and C10, (left) melting process, (right) solidification process.
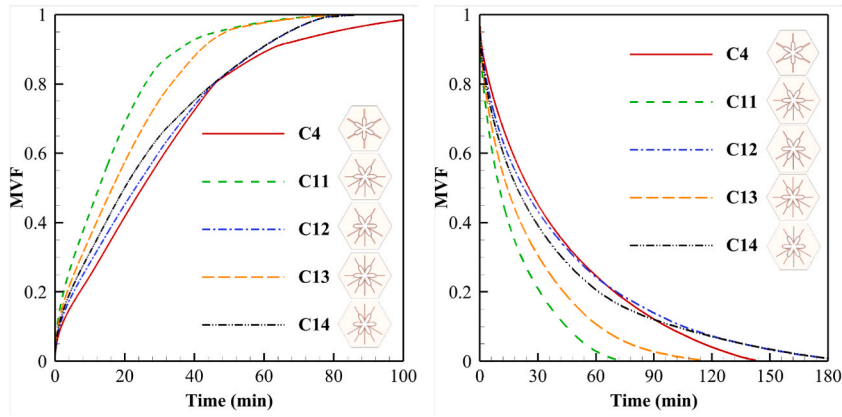

Fig. 11. Temporal variation of melting volume fraction for C4, and C11-C14, (left) melting process, (right) solidification process.

is similar to the C11, except that it has one more fin. However, the C12 and C14 cases have a significant difference from the C11. This is because the C11 and C13 cases have two horizontal fins that provide more heat dissipation, while the C12 and C14 cases do not have horizontal fins. Moreover, Fig. 12 depicts the temporal variations of melting volume fraction for four cases C6, C7, C15, and C16 with symmetrical fin configurations. In cases C15 and C16, a better performance is observed than C6 and C7. It can be inferred that increasing the fin numbers improves the melting and solidification rates. Meanwhile, the difference between C15 and C16 is 30 degrees of rotation, which has minimal impact on the thermal performance of the system.

It should be noted that in cases C4 and C5, the orientation of the fins plays a role in influencing melting and solidification times. In
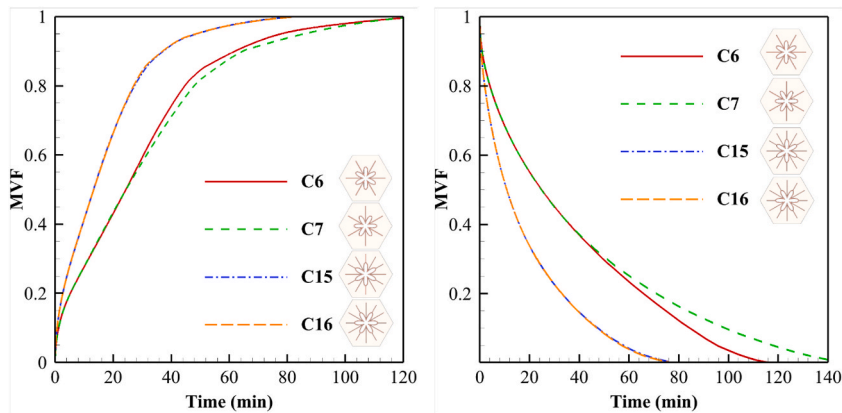

Fig. 12. Temporal variation of melting volume fraction for C6, C7, C15, and C16, (left) melting process, (right) solidification process.

both configurations, the fins are positioned at the top of the petals. However, C5 provides improved heat uniformity at the bottom region due to its rotated arrangement, which helps direct more heat to areas typically limited by weaker convection. In contrast, for cases like C15 and C16, where multiple long fins are distributed around the enclosure, the effect of rotation becomes less significant. As the petals and fins rotate, another set of long fins naturally replaces the previous ones in the lower region, maintaining a similar level of heat distribution. This consistent coverage ensures that the thermal performance at the bottom remains nearly unchanged regardless of orientation. In essence, when fewer or asymmetrically placed fins are used, as in C4 and C5, rotation can impact how effectively different regions are heated or cooled. However, in configurations with numerous evenly distributed long fins, like C15 and C16, the overall heat transfer performance remains stable, making rotation less critical.

Finally, by comparing C15 and C11 cases, it is concluded that the case C11 has the best performance compared to other cases, so that at $t = 40$ min, for the case C1,1 MVF = 94 % (see Fig. 11) and for case C15 MVF = 91 %, in the melting process.

It is important to note that the total mass of fins is fixed; therefore, adding extra fins necessitates reducing the thickness of all fins. As a result, strategic placement of fins becomes essential to enhance heat transfer, both by supporting natural convection and ensuring well-distributed thermal conduction. Simply increasing the number of fins without considering their positioning can be counterproductive. A comparison between cases C11 and C13 highlights this point. In C13, an additional fin is placed at the top of the enclosure. However, this region already benefits from strong natural convection, and the added fin offers minimal additional thermal benefit. More critically, the redistribution of material to accommodate the extra fin results in thinner fins elsewhere—particularly in regions where heat transfer support is more urgently needed.

This thinning reduces the overall effectiveness of the heat conduction path, leading to a net decline in thermal performance. In contrast, C11 demonstrates more efficient fin placement, prioritizing areas with weaker convection, such as the bottom of the enclosure. This targeted strategy maximizes the utility of the fixed fin mass, balancing convection-driven and conduction-driven heat transfer, and ultimately improving both melting and solidification efficiency.

Interestingly, case C4 demonstrates strong phase change performance during the early and middle stages; however, its advantage diminishes significantly in the later stages. This is due to the limited total fin mass—placing fins primarily in the top region provides a temporary benefit by accelerating melting in that area. As the process continues and natural convection becomes more dominant, the upper regions are already fully melted, while the lower regions, where convection is weaker, lack sufficient fins to sustain efficient heat transfer. As a result, C4 loses its thermal advantage in the later stages of the phase change process.

In the final analysis, the thermal performance of the C11 is compared to three finless cases including a 6-Pl (C17), a 6-Pl with a 30° rotation (C18), and a circular cross-section as the baseline case (C19). Fig. 13 shows the temporal variations of melting volume fraction of these cases. It is clear that the baseline case has the weakest performance compared to the other cases, because it has a very small heat transfer area. According to the results of the cases examined, the C11 is selected as an optimal configuration. In addition, Fig. 14 illustrates the MVF contours along with the liquid PCM streamlines at t = 40 min for C11, C15, C17, and C19 cases. In the cases of C11, a large volume of PCM is melted for the melting process while, the baseline case has the minimum melting volume fraction. For the solidification process, again C11 shows the best performance. Moreover, in order to investigate the temperature distribution in the solution field, the contours of temperature difference of PCM ($\Delta T = T\text{-}T_c$) along with isotherm lines are shown in Fig. 15 for the melting and solidification processes at $t = 40$ min. As expected, the temperature in C11 is more spread out, while in the baseline case the temperature is concentrated in the areas adjacent to the tube.

Fig. 14 illustrates that long fins generate localized natural convection circulations between themselves during the early stages of melting. As melting progresses toward the tips of the fins and beyond, these individual convection loops begin to merge, forming larger, global circulation patterns. This transition helps distribute heat more effectively and accelerates the melting of the remaining PCM near the enclosure's outer edges. While long fins may initially suppress large-scale convection by segmenting the melt region, their conductive pathways compensate during the final, conduction-dominated stage, supplying residual PCM interfaces with heat from multiple directions and ensuring efficient completion of the phase change. In the solidification process, these long uniform fins also play a beneficial role. They form an extensive and well-connected thermal network that enhances conductive heat transfer
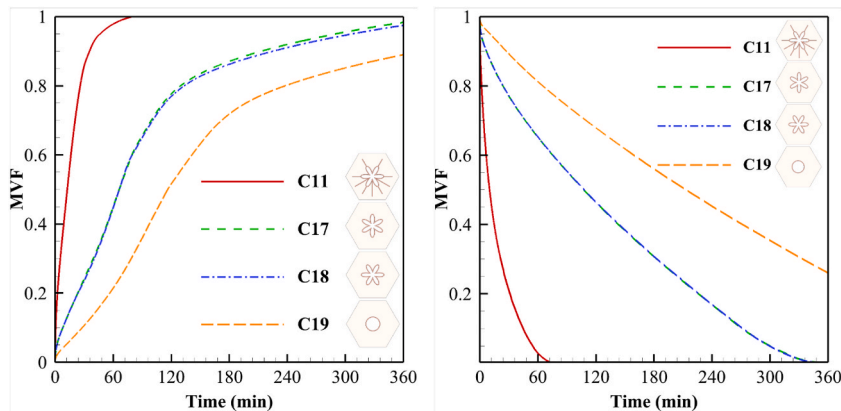

Fig. 13. Temporal variation of melting volume fraction for C11, and C17-C19, (left) melting process, (right) solidification process.
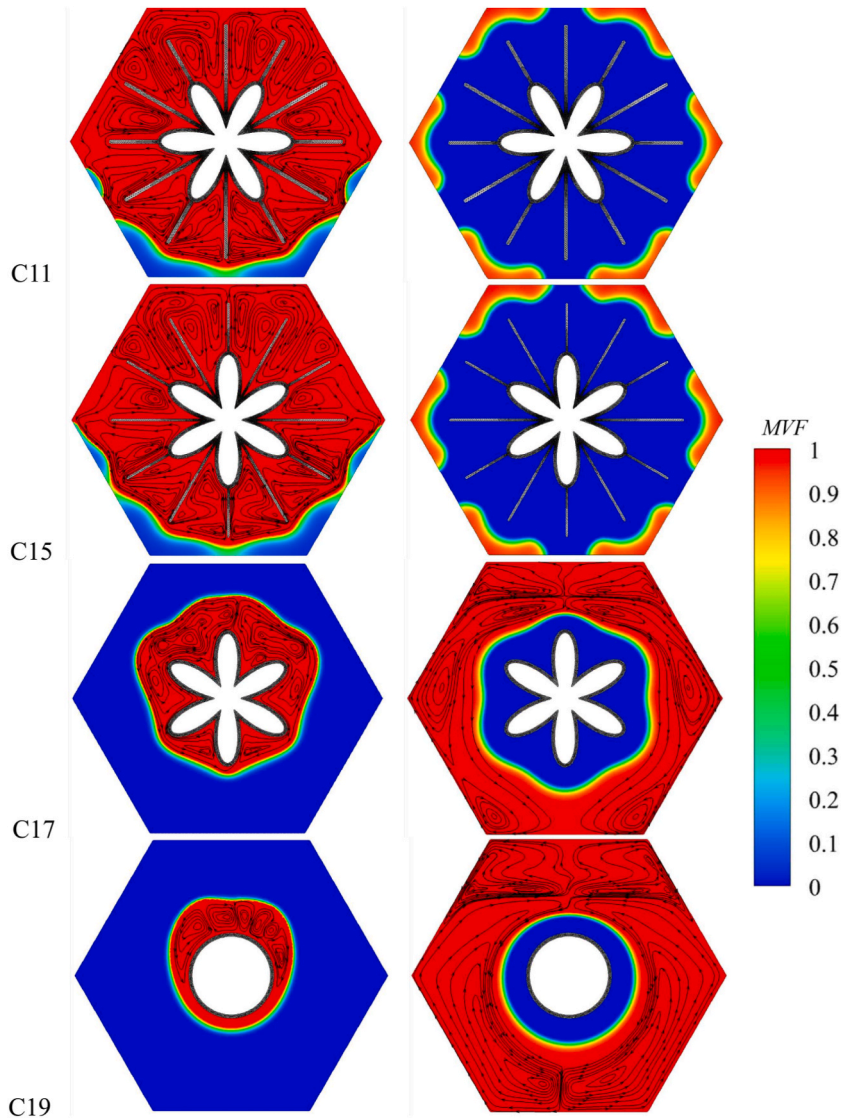
Fig. 14. Contours of MVF along with the liquid PCM streamlines at $t = 40$ min for C11, C15, C17, and C19, (Left) melting process, (Right) solidification process.

throughout the PCM. This web-like structure promotes a more uniform solidification front and supports better overall thermal performance, especially in the absence of strong convection. Meanwhile, weak natural convection effects that persist during solidification tend to be confined to the edges of the hexagonal enclosure. The long fins guide heat flow effectively inward from these regions, helping to reduce temperature gradients and limit the formation of cold, stagnant zones.

In case C19, melting begins solely around the heated central tube, and natural convection develops only after a small liquid region has formed. This results in a slow and localized heat transfer process. However, when a petal-shaped tube is introduced, the initial molten region becomes noticeably larger, and the melt spreads more rapidly along the petal surfaces, leading to a significantly expanded liquid zone early in the process. The addition of fins further enhances this effect by distributing heat more effectively throughout the PCM domain. The fins act as thermal bridges, transferring heat deeper into the PCM and rapidly forming a wider molten region. Localized natural convection currents also develop between the fins, eventually merging into broader flow patterns. This merging marks the transition from conduction-dominated melting to convection-enhanced melting. Once large-scale circulation develops, heat is redistributed more uniformly across the PCM domain, reducing temperature gradients and accelerating melting in previously conduction-limited regions. As a result, the presence of fins significantly accelerates the melting process, particularly in the regions between fins. During solidification, petal-shaped tubes enhance cooling around the petal surfaces, promoting faster formation of solid PCM compared to a plain tube. This creates a more extensive solid region in the early stages. When fins are present, they extract heat from the surrounding liquid PCM efficiently, enabling a large portion of the domain to solidify more quickly. However, once solid PCM forms around the fins, it begins to act as an insulating layer. This slows down heat transfer to the remaining liquid PCM between
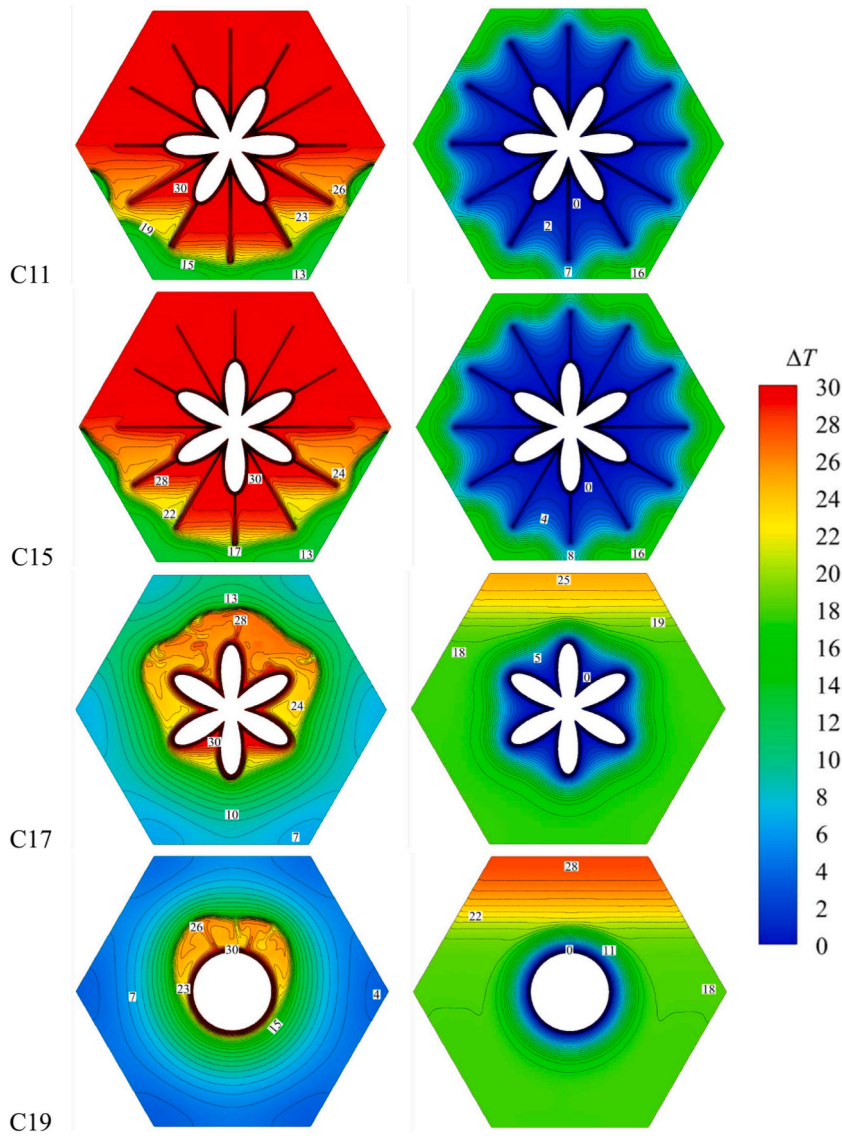
Fig. 15. Contours of temperature at $t = 40$ min for C11, C15, C17, and C19, (Left) melting process, (Right) solidification process.

the fins and the outer hexagon shell. Consequently, the rate of solidification decreases in these peripheral regions, as the growing solid mass increases thermal resistance and limits further heat extraction.

The data in Tables 3 and in addition to the geometric characteristics of the cases, include the time to reach a melting fraction of 0.9 for the melting state and a melting fraction of 0.1 for the solidification state. Figs. 16 and 17 show bar charts of the phase change time.

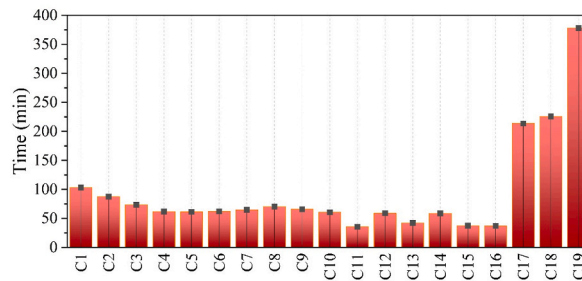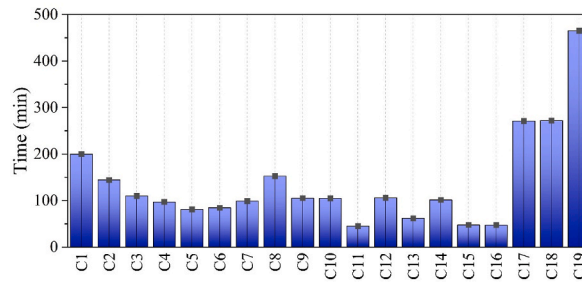**Fig. 16.** Bar chart of melting process duration to reach MVF = 0.9.

Fig. 17. Bar chart of solidification process duration to reach MVF = 0.1.

The cases C11, C16, C15, and C13 rank first to fourth for the best configurations for both melting and solidification, respectively. In contrast, the cases C19, C18, C17, and C1 have the worst configurations. For a melting case at MVF = 0.9, the stored total energy is about 888 kJ/m. The energy storage rate (Q) can be computed as Q = Stored energy/Time. For the best case, C11, the energy storage rate is about 412 W. The literature studies for lobed structures provide 228.3 W [11]. While a direct numerical comparison is limited because of differences in PCM mass, geometry, and system dimensions, both results fall within the same performance scale. This suggests that petal-shaped tubes with asymmetric fins can provide competitive thermal performance compared to previously reported lobed-shell configurations.

5. Conclusions

The free convection flow and heat transfer of PCMs in a hexagon LHTES unit including a petal shape HTF tube with attached fins. The porosity-enthalpy method was applied to model the phase change in the enclosure. The FEM was employed to solve the governing equations. The mass of utilized fins was kept constant while their configurations was changed. The symmetric and asymmetric fins were investigated. The results were reported in tables and graphs. The contours of liquid fraction, temperatures and streamlines were reported to highlight the phase change behavior of the system. The main findings can be listed as follows:

- The study evaluated 19 LHTES configurations, revealing that increasing the number of petals and optimizing fin placement dramatically enhances melting and solidification rates. For instance, increasing petals from 3 to 6 reduced melting time by approximately 41 % (C1 to C4). Among all cases, C11, C15, and C16 showed the highest efficiency—achieving up to 90 % reduction in both melting and solidification times compared to the baseline (C19).
- Asymmetrical fin configurations, especially those targeting the lower enclosure regions, significantly improved melting by supporting heat transfer where natural convection is weakest. These fins also accelerated solidification in the early and middle stages by increasing contact area. However, their benefit diminishes in later stages due to uneven thermal resistance, which slows down complete solidification.
- Cases like C15 and C16, which used many long, uniformly distributed fins, maintained strong performance throughout the melting and solidification processes. These fins promoted localized and eventually global convection loops during melting, while forming a conductive network during solidification. Importantly, fin rotation had little effect in these cases due to the symmetrical and redundant fin layout.
- Among all configurations, C11 consistently delivered the best results, achieving 94 % melting at 40 min and outperforming both finless and symmetric cases. Its fin arrangement offered superior thermal coverage, especially in low-convection zones. In contrast, cases with too many or poorly positioned fins (e.g., C13) saw reduced performance due to thinner fins and inefficient heat distribution.
- The circular, finless baseline case (C19) had the longest melting and solidification times due to minimal surface area and weak natural convection development. In contrast, petal-shaped enclosures and well-designed fins greatly expanded the initial melt zone, improved convective mixing, and enhanced heat conduction. This underscores the importance of shell geometry and targeted fin design in PCM-based thermal energy storage.

In conclusion, the findings of this study demonstrate that the use of petal-shaped tubes, combined with strategically engineered fin designs, holds significant potential for enhancing the thermal performance of LHTES systems. These geometric modifications can substantially improve heat transfer rates during both the charging and discharging phases. By increasing the efficiency and responsiveness of thermal energy storage, such advancements contribute to more effective integration of renewable energy sources. Ultimately, these improved LHTES configurations can support the development of sustainable energy solutions for both residential and industrial applications, helping to reduce dependence on conventional energy systems and lower overall carbon emissions.

The results showed that the placement and arrangement of fins can notably influence phase change heat transfer. Both the natural convection effects and the distributed surface of the fins played important roles in the phase change processes. Overall, the results highlight three broader design principles for LHTES optimization: (i) shell geometry strongly influences convective flow development, with petal-shaped tubes outperforming circular baselines; (ii) fin configuration, particularly asymmetrical placement, can deliberately

guide convection and enhance uniformity; and (iii) maintaining constant fin mass while optimizing distribution ensures balanced improvements in both melting and solidification. These principles provide generalizable insights for the design of compact, high-performance storage units beyond the specific cases investigated here.

Future studies can consider analyzing the vertical shifting of the petal-shaped tubes and fins toward the bottom to allow better natural convection. Additionally, the shell tubes were considered insulated; however, it is also possible to place the shells in a bundled formation without insulation. The bundle effects can be considered in future studies using thermal periodic boundary conditions.

CRediT authorship contribution statement

Fathi Alimi: Writing – review & editing, Writing – original draft, Methodology, Investigation, Formal analysis, Conceptualization. **Khalil Hajlaoui:** Writing – review & editing, Writing – original draft, Supervision, Methodology, Investigation, Formal analysis, Conceptualization. **Mohamed Bouzidi:** Writing – review & editing, Writing – original draft, Project administration, Methodology, Investigation, Formal analysis. **Mansour Mohamed:** Writing – review & editing, Writing – original draft, Methodology, Investigation, Formal analysis. **Wahiba Yaïci:** Writing – review & editing, Writing – original draft, Methodology, Investigation, Formal analysis. **Nashmi H. Alrasheedi:** Writing – review & editing, Writing – original draft, Investigation, Formal analysis, Conceptualization. **Mohammad Ghalambaz:** Writing – review & editing, Writing – original draft, Validation, Supervision, Project administration, Methodology, Investigation, Formal analysis, Conceptualization. **Pouyan Talebidadehsardari:** Writing – review & editing, Writing – original draft, Supervision, Software, Methodology, Investigation, Formal analysis, Conceptualization.

Funding

Declaration of competing interest

The authors declare that they have no known competing financial interests or personal relationships that could have appeared to influence the work reported in this paper.

Data availability

Data will be made available on request.

References

[1] P. Gadhave, F. Pathan, S. Kore, C. Prabhune, Comprehensive review of phase change material based latent heat thermal energy storage system, Int. J. Ambient Energy 43 (1) (2022) 4181–4206.
[2] V.H.U. Eze, J.S. Tamball, O. Robert, W. Okafor, Advanced modeling approaches for latent heat thermal energy storage systems, IAA J. Appl. Sci. 11 (1) (2024) 49–56.
[3] Z.H. Low, Z. Qin, F. Duan, A review of fin application for latent heat thermal energy storage enhancement, J. Energy Storage 85 (2024) 111157.
[4] S. Tian, J. Ma, S. Shao, Q. Tian, Z. Wang, Y. Zhao, B. Tan, Z. Zhang, Z. Sun, Estimation of heat transfer performance of latent thermal energy storage devices with different heat transfer interface types: a review, J. Energy Storage 86 (2024) 111315.
[5] M. Boujelbene, S.A. Mehryan, M. Sheremet, M. Shahabadi, N.B. Elbashir, M. Ghalambaz, Numerical study of a Non-Newtonian phase change flow in finned rectangular enclosures, facta universitatis, Series: Mech. Eng. 23 (2025) 287–310.
[6] A. Agrawal, D. Rakshit, Review on thermal performance enhancement techniques of latent heat thermal energy storage (LHTES) system for solar and waste heat recovery applications. New Research Directions in Solar Energy Technologies, 2021, pp. 411–438.
[7] W. Ye, J. Khodadadi, Effects of arrow-shape fins on the melting performance of a horizontal shell-and-tube latent heat thermal energy storage unit, J. Energy Storage 54 (2022) 105201.
[8] R. Hamid, Z. Mehrdoost, Thermal performance enhancement of multiple tubes latent heat thermal energy storage system using sinusoidal wavy fins and tubes geometry modification, Appl. Therm. Eng. 245 (2024) 122750.
[9] X. Cai, Z.J. Zheng, C. Yang, Y. Xu, Improving the solidification performance of a shell-and-tube latent-heat thermal energy storage unit using a connected-y-shaped fin, Int. J. Energy Res. 46 (9) (2022) 12758–12771.
[10] K. Sudarmozhi, D. Iranian, N. Alessa, Investigation of melting heat effect on fluid flow with brownian motion/thermophoresis effects in the occurrence of energy on a stretching sheet, Alex. Eng. J. 94 (2024) 366–376.
[11] A. NematpourKeshteli, M. Iasiello, G. Langella, N. Bianco, Optimization of the thermal performance of a lobed triplex-tube solar thermal storage system equipped with a phase change material, Heliyon 10 (16) (2024) e36105.
[12] S. Mousavi, M. Sheikholeslami, Enhancement of solar evacuated tube unit filled with nanofluid implementing three lobed storage unit equipped with fins, Sci. Rep. 14 (1) (2024) 7939.
[13] C. Ding, J. Pei, S. Wang, Y. Wang, Evaluation and comparison of thermal performance of latent heat storage units with shell-and-tube, rectangular, and cylindrical configurations, Appl. Therm. Eng. 218 (2023) 119364.
[14] N.B. Khedher, N. Biswas, H. Togun, H.I. Mohammed, J.M. Mahdi, R.K. Ibrahem, P. Talebizadehsardari, Geometry modification of a vertical shell-and-tube latent heat thermal energy storage system using a framed structure with different undulated shapes for the phase change material container during the melting process, J. Energy Storage 72 (2023) 108365.
[15] N.S. Bondareva, M.A. Sheremet, A numerical study of heat performance of multi-PCM brick in a heat storage building, Mathematics 11 (13) (2023) 2825.
[16] A. Kazemian, K. Khosravi, S. Sen, P. Talebizadehsardari, A. Cairns, T. Ma, Optimizing photovoltaic thermal systems with wavy collector tube: a response surface-based design study with desirability analysis, Appl. Therm. Eng. 258 (2025) 124475.
[17] S.B. Oskouei, Ö. Bayer, Performance improvement in a vertical latent thermal energy storage tank with crossing heat transfer tubes, J. Energy Storage 88 (2024) 111504.

[18] Z. Cheng, J. Du, S. Jia, C. Xiao, F. Jiao, Y. Hong, Impact of tube shapes on the energy storage and thermal-hydraulic performances of finned latent heat energy storage systems, Case Stud. Therm. Eng. (2025) 105827.

[19] M.A. Said, H. Togun, A.M. Abed, N. Biswas, H.I. Mohammed, H.S. Sultan, J.M. Mahdi, P. Talebizadehsardari, Evaluation of wavy wall configurations for accelerated heat recovery in triplex-tube energy storage units for building heating applications, J. Build. Eng. 94 (2024) 109762.

[20] M. Ghalambaz, S. Mehryan, A. Veismoradi, M. Mahdavi, I. Zahmatkesh, Z. Kazemi, O. Younis, M. Ghalambaz, A.J. Chamkha, Melting process of the nano-enhanced phase change material (NePCM) in an optimized design of shell and tube thermal energy storage (TES): taguchi optimization approach, Appl. Therm. Eng. 193 (2021) 116945.

[21] S.D. Farahani, A.D. Farahani, A.J. Mamoei, H.F. Öztop, Scrutiny of melting rate of phase change material in a four petals cavity with internal branch fins under magnetic field, J. Magn. Magn Mater. 575 (2023) 170727.

[22] M.K. Nayak, A.S. Dogonchi, A. Rahbari, Free convection of Al2O3-water nanofluid inside a hexagonal-shaped enclosure with cold diamond-shaped obstacles and periodic magnetic field, Case Stud. Therm. Eng. 50 (2023) 103429.

[23] S.B. Oskouei, Z.-R. Li, Ö. Bayer, L.-W. Fan, Close-contact melting and natural convection in unconstrained melting: a parametric study, Int. J. Heat Mass Tran. 218 (2024) 124795.

[24] S. Wu, X. Zhang, K. Tang, T. Li, Magnetically-regulated close contact melting for high-power-density latent heat energy storage, J. Energy Storage 95 (2024) 112660.

[25] Y. Huang, H. Zhai, C. Zhang, An efficient thermal buffer utilizing pressure-driven close-contact melting, Int. J. Heat Mass Tran. 249 (2025) 127225.

[26] I. Salman, T. Shockner, R.A. Stavins, S. Kim, E. Koronio, O. Gal, M.S. Spector, W.P. King, N. Miljkovic, G. Ziskind, A "hourglass" system for transient thermal management based on dynamic close-contact melting of a phase-change material, Int. J. Heat Mass Tran. 239 (2025) 126542.

[27] M. Ezra, Y. Kozak, The influence of thermal convection in the thin molten layer on close-contact melting processes, Int. J. Heat Mass Tran. 235 (2024) 126184.

[28] Nishiyama's heat exchangers?featuring technology for improved heat transfer performance, in: Nishiyama Seisakusho Co, 2025.

[29] S. Zhang, Y. Yao, Y. Jin, Z. Shang, Y. Yan, Heat transfer characteristics of ceramic foam/molten salt composite phase change material (CPCM) for medium-temperature thermal energy storage, Int. J. Heat Mass Tran. 196 (2022) 123262.

[30] M. Ghalambaz, A.A. Melaibari, A.J. Chamkha, O. Younis, M. Sheremet, Phase change heat transfer and energy storage in a wavy-tube thermal storage unit filled with a nano-enhanced phase change material and metal foams, J. Energy Storage 54 (2022) 105277.

[31] D.A. Nield, A. Bejan, Convection in Porous Media, Springer, 2006.

[32] B. Kamkari, H.J. Amlashi, Numerical simulation and experimental verification of constrained melting of phase change material in inclined rectangular enclosures, Int. Commun. Heat Mass Tran. 88 (2017) 211–219.

[33] I. Benyahia, M.F. Al-Ghamdi, A. Abderrahmane, O. Younis, S. Laouedj, K. Guedri, A. Alahmer, Comprehensive thermal analysis of a nano-enhanced PCM in a finned latent heat storage system, Int. Commun. Heat Mass Tran. 165 (2025) 109106.

[34] R. Karami, B. Kamkari, Investigation of the effect of inclination angle on the melting enhancement of phase change material in finned latent heat thermal storage units, Appl. Therm. Eng. 146 (2019) 45–60.

[35] S. Arena, E. Casti, J. Gasia, L.F. Cabeza, G. Cau, Numerical simulation of a finned-tube LHTES system: influence of the mushy zone constant on the phase change behaviour, Energy Proc. 126 (2017) 517–524.

[36] C. Zhao, J. Wang, Y. Sun, S. He, K. Hooman, Fin design optimization to enhance PCM melting rate inside a rectangular enclosure, Appl. Energy 321 (2022) 119368.

[37] A.I.N. Korti, H. Guellil, Experimental study of the effect of inclination angle on the paraffin melting process in a square cavity, J. Energy Storage 32 (2020) 101726.

[38] A. Agarwal, R. Sarviya, Characterization of commercial grade paraffin wax as latent heat storage material for solar dryers, Mater. Today Proc. 4 (2) (2017) 779–789.

[39] N. Ukrainczyk, S. Kurajica, J. Šipušić, Thermophysical comparison of five commercial paraffin waxes as latent heat storage materials, Chem. Biochem. Eng. Q. 24 (2) (2010) 129–137.

[40] H. Zheng, C. Wang, Q. Liu, Z. Tian, X. Fan, Thermal performance of copper foam/paraffin composite phase change material, Energy Convers. Manag. 157 (2018) 372–381.

[41] O.C. Zienkiewicz, R.L. Taylor, P. Nithiarasu, The Finite Element Method for Fluid Dynamics, seventh ed., Butterworth-Heinemann, Oxford, 2014.

[42] D. Pepper, The Intermediate Finite Element Method: Fluid Flow and Heat Transfer Applications, Routledge, 2017.

[43] C.T. Kelley, Solving Nonlinear Equations with Newton's Method, SIAM, 2003.

[44] P. Deuflhard, Newton Methods for Nonlinear Problems: Affine Invariance and Adaptive Algorithms, Springer Science & Business Media, 2005.

[45] M. Bollhöfer, O. Schenk, R. Janalik, S. Hamm, K. Gullapalli, State-of-the-art sparse direct solvers. Parallel Algorithms in Computational Science and Engineering, 2020, pp. 3–33.

[46] M. Bollhöfer, A. Eftekhari, S. Scheidegger, O. Schenk, Large-scale sparse inverse covariance matrix estimation, SIAM J. Sci. Comput. 41 (1) (2019) A380–A401.

[47] M. Boujelbene, H.S. Sultan, S. Mehryan, A.M. Hussin, A.S. Alghawli, M. Ghalambaz, Analyzing the melting process in a tilted heat sink filled with a phase change material equipped with the plate and optimized tree-shaped metal fins, J. Energy Storage 92 (2024) 111608.

[48] N.A. Qasem, A. Abderrahmane, A. Belazreg, O. Younis, Y. Khetib, K. Guedri, Investigation of phase change heat transfer in a rectangular case as function of fin placement for solar applications, Case Stud. Therm. Eng. 54 (2024) 103996.

[49] B. Kamkari, H. Shokouhmand, F. Bruno, Experimental investigation of the effect of inclination angle on convection-driven melting of phase change material in a rectangular enclosure, Int. J. Heat Mass Tran. 72 (2014) 186–200.

[50] B. Kamkari, D. Groulx, Experimental investigation of melting behaviour of phase change material in finned rectangular enclosures under different inclination angles, Exp. Therm. Fluid Sci. 97 (2018) 94–108.

[51] M. Bouzidi, M. Sheremet, M. Shank, S. Tiari, M. Ghalambaz, Charging and discharging heat transfer improvement of shell-tube storage utilizing a partial layer of anisotropic metal foam, J. Energy Storage 79 (2024) 109948.

[52] A. Alasmari, H.S.S. Aljibori, F. Alimi, M. Bouzidi, M.S. Islam, S. Yazdani, M. Ghalambaz, A shell-tube latent heat thermal energy storage: influence of metal foam inserts in both shell and tube sides, Int. Commun. Heat Mass Tran. 159 (2024) 107992.